LAWRENCE
LIVERMORE
NATIONAL
LABORATORY

LLNL-JRNL-405025

# Numerical Simulations of Pillar Structured Solid State Thermal Neutron Detector Efficiency and Gamma Discrimination

A. Conway, T. Wang, N. Deo, C. Cheung, R. Nikolic

June 30, 2008

Transactions on Nuclear Science

## Disclaimer

# Numerical Simulations of Pillar Structured Solid State Thermal Neutron Detector: Efficiency and Gamma Discrimination

A. M. Conway, *Member, IEEE*, T. F. Wang, N. Deo, C. L. Cheung, R. J. Nikolic, *Member, IEEE*

**Abstract— This work reports numerical simulations of a novel three-dimensionally integrated, $^{10}$boron ($^{10}$B) and silicon p+, intrinsic, n+ (PIN) diode micropillar array for thermal neutron detection. The inter-digitated device structure has a high probability of interaction between the Si PIN pillars and the charged particles (alpha and $^{7}$Li) created from the neutron – $^{10}$B reaction. In this work, the effect of both the 3-D geometry (including pillar diameter, separation and height) and energy loss mechanisms are investigated via simulations to predict the neutron detection efficiency and gamma discrimination of this structure. The simulation results are demonstrated to compare well with the measurement results. This indicates that upon scaling the pillar height, a high efficiency thermal neutron detector is possible.**

**Index Terms— Monte Carlo simulation, neutron detector, semiconductor device modeling, solid state detectors**

## I. Introduction

NEUTRON detectors are needed for applications ranging from homeland security to particle physics and astronomy. Solid state detectors have advantages over the currently used $^{3}$helium ($^{3}$He) gas based technology in their inherent insensitivity to microphonics, low voltage operation and small device footprint. This has lead to a variety of semiconductor based thermal neutron detectors, which include the use of various neutron conversion materials and both 2-D and 3-D geometries [1-4].

Since thermal neutrons have a low probability of interacting with conventional semiconductor materials, a two-step detection process to produce electrical signals is generally employed. First, the thermal neutrons are converted to energetic ions by a material with a high thermal neutron cross-section. In this work, $^{10}$B (cross-section, $\sigma$ = 3837 barns) is used resulting in the following reaction: n + $^{10}$B → α + $^{7}$Li. Second, these ions are collected using a reverse biased semiconductor diode. A Si PIN structure was used for the semiconductor diode. Two major criteria that drive the optimal design of thermal neutron detectors are: sufficient thickness of neutron convertor material (~54 μm in $^{10}$B) and high probability of ion energy deposition within semiconductor detector (ion track length = 3.6 μm in $^{10}$B, for the most energetically favorable reaction) [5]. Using a three-dimensionally integrated approach, the design of very high detection efficiency solid state neutron detector using the converter material concept is possible because the geometrical constraints on the converter material thickness are largely decoupled from the limitation of the ion track length. A schematic diagram of our detector is shown in Figure 1, In this case, the $^{10}$B thickness is defined by the pillar height (etch depth) to absorb the neutron flux. The pillar pitch is defined lithographically to allow the highest possible interaction of the energetic ions with the semiconductor pillars.

Previous work in the area of simulations has primarily included the Monte Carlo simulations for the neutron histories and the by-product range calculations for the efficiency predictions [2, 4]. Analogous methodologies for efficiency optimization have been applied to microchannel plates using a $^{10}$B doped glass structure [6]. In this work, the neutron and by-product calculation is coupled with the effect of electrical transport within the semiconductor detector for our novel 3-D pillar geometry [7-9]. This improvement allows more accurate simulation of the thermal neutron detection efficiency for a semiconductor based 3D neutron detector, along with gamma discrimination and the effect of the pillar geometry (pillar diameter, separation and height).

## II. Simulation Methodology

To calculate the efficiency of thermal neutron detection and discrimination between gamma events and neutron events, 3-D numerical simulations were performed. The detection efficiency for a solid-state neutron detector is given by:

$$Efficiency = \eta_{\text{int}} \cdot \eta_{conv} \cdot \eta_{semi} \cdot \eta_{rec} = \frac{Counts > Threshold}{\#\ IncidentNe utrons} \quad (1)$$

where $\eta_{int}$ is the probability of neutron interaction with $^{10}$B, $\eta_{conv}$ is the probability that energetic ions reach semiconductor detector, $\eta_{semi}$ is the probability that energetic ions deposit enough energy in the semiconductor, and $\eta_{rec}$ is the efficiency reduction factor due to charge carrier recombination. The simulations were broken into four corresponding parts: the neutron-$^{10}$B reaction, energy loss of the reaction products within the $^{10}$B, deposition of energy in the Si pillars to create electron-hole pairs, and then recombination of these carriers in the Si pillars. The effect of pillar diameter, spacing and height were explored. The following subsections discuss each

Manuscript received July 3, 2008 This work performed under the auspices of the U.S. Department of Energy by Lawrence Livermore National Laboratory under Contract DE-AC52-07NA27344, LLNL-JRNL-405025.

A. M. Conway, T. F. Wang and R. J. Nikolic are with Lawrence Livermore National Laboratory, Livermore, CA 94550 USA (e-mail: conway8@llnl.gov, wang6@llnl.gov, nikolic1@llnl.gov).

N. Deo and C. L. Cheung are with the Department of Chemistry, University of Nebraska, Lincoln, NB (email: ndeo@unl.edu, ccheung@unl.edu).

efficiency component and method used in details.

### A. Neutron-$^{10}B$ Interaction Simulation ($\eta_{int}$)

The probability that a neutron interacts with a material, $\eta_{int}$, is determined by the formula [10]:

$$\eta_{\text{int}} = 1 - e^{\frac{-t}{mfp}} \quad (2)$$

where t is the thickness of the layer and mfp is the mean free path of a neutron in $^{10}B$. Monte Carlo N Particle transport code (MCNP) [11] was used to calculate the neutron interaction histories as well as the secondary particle trajectories within the pillar array. The thermal neutron - $^{10}B$ reaction is as follows:

$$1^{st} \text{ excited state: } {}^{10}B + n \rightarrow \alpha + {}^{7}Li + \gamma$$

$$\text{Ground state: } {}^{10}B + n \rightarrow \alpha + {}^{7}Li$$

where the ground state has a probability of occurring 6% of the time and the first excited state has a probability of occurring 94% of the time. Both the ground state and the first excited state were simulated. It was assumed that the 0.4776 MeV gamma photon generated by the 1st excited state reaction escapes from the detector without interacting. A 5 mm x 5 mm array of pillars was used for the MCNP simulations with neutrons incident on all sides ($4\pi$) of the array at all possible angles (Figure 2). Approximately $10^{10}$ interaction histories were simulated and recorded.

### B. Energy deposition rate of ions in structure ($\eta_{con}$, $\eta_{semi}$)

The energy lost by the reaction by products in the $^{10}B$ portion and deposited in the Si portion of the detector was tracked for each event using an energy dependent change in energy per unit distance (dE(E)/dx). To calculate dE/dx for alpha and $^{7}Li$ in both the $^{10}B$ and Si portions of the detector, the Monte Carlo program Stopping Range of Ions in Matter (SRIM) [12] was used. Figure 3 shows the dE/dx and range of both ionized alpha and $^{7}Li$ particles in silicon as a function of energy. Lateral and longitudinal straggling was neglected in the simulation. Table 1 shows the average range of reaction by-products in $^{10}B$ and Si for the both the ground state and 1st excited state.

### C. Electrical transport in Si Pillars ($\eta_{rec}$)

A commercially available 3-D finite element TCAD software package (Silvaco's Atlas) was applied to calculate the transport of the electrons and holes generated by the alpha and $^{7}Li$ particles in the Si diode portion of the detector. The amount of energy deposited in the Si pillar by either the $^{7}Li$ and/or alpha was converted to an electron-hole pair generation rate. This rate was computed by dividing the energy lost taken from the coupled MCNP/SRIM simulation by the ionization energy of Si (3.6 eV [13, 14] ) and converted to a rate per volume by assuming a track diameter of 0.1 μm [15] . The generation rate as a function of position was input into a 3-D transient simulation to determine the output current pulse for a variety of input conditions. A subset of possible incident energies and heights were used to calculate the amount of carrier recombination and the efficiency reduction factors for each simulation. The amount of energy deposited in the Si pillars for each event was then multiplied by the appropriate efficiency reduction factor to determine the total deposited energy for each event. An electric field dependent mobility model was used along with Shockley-Read-Hall model for bulk recombination and surface recombination along the edges of the pillars. The effect of carrier lifetimes and surface recombination velocities on carrier recombination for a 1.47 MeV alpha (which corresponds to the energy of the resulting alpha from the most probably neutron - $^{10}B$ interaction) normally incident on the center of the pillar was also investigated.

### D. Efficiency calculation

The detection efficiency of the proposed device was determined by dividing the number of interaction events that resulted in a collected energy above the minimum threshold of 100 keV by the total number of neutrons generated from the source.

### E. Gamma Discrimination Simulation

The gamma-ray detection efficiency is simulated in similar fashion to the neutron detection efficiency determination described in the above "Neutron-$^{10}B$ Interaction Simulation" section. A simpler energy tally (already built in the MCNP, the F8 tally [11]) was used. Instead of thermal neutrons, incident gamma-ray energies of 200 keV, 662 keV and 1 MeV were used.

## III. Results and Discussion

Based on the simulation methodology presented in Section II, various geometries of the pillar structured thermal neutron detector based on the architecture shown in Figure 1 were simulated. The structures consisted of pillar geometries of with diameters and spacings of 1 μm x 1μm, 2 μm x 2 μm and 5 μm x 5 μm, configured in a square lattice geometry (Figure 2). The pillar height was varied from 10 to 100 μm. Figure 2 shows the neutron flux set-up used for the neutron history simulation. Owing to the random nature of the interactions of the neutrons with the $^{10}B$ and the trajectory of the reaction by products (alpha and $^{7}Li$ ions), the spectroscopic information is lost. However, the detection of thermal neutrons does not require spectroscopic information of the reaction by-products, only their presence, which is determined by registering a count above a predetermined energy threshold. This threshold is set by the noise floor of the detector which is dominated by leakage current. Nonetheless, it can also be affected by cosmic rays and gamma rays, though generally to a lesser degree (Figure 3). Actually, as will be shown in the "Gamma Rejection" subsection below, the effect of gamma ray interaction is negligible for our structure. Since increasing the energy threshold reduces the detection efficiency by discarding low energy counts, leakage current is an important device

parameter for high thermal neutron detection efficiency. The following sub-sections discuss the simulation results.

### A. Surface recombination velocity and lifetime effects

Once the reaction by-products deposit energy in the Si pillar and generate electron-hole pairs (ehp), these carriers are then transported to the electrical contacts to create a current pulse via an externally applied electric field. These carriers can recombine during transport and thus reduce the current pulse. Two recombination mechanisms are dominant: Shockley-Read-Hall (SRH) recombination via defect states within the Si pillars and surface recombination around the edges of the pillars. Radiative recombination is not a dominant factor for indirect bandgap semiconductors such as Si. The effect of carrier lifetimes on carrier transport is shown in Figure 4. For typical values of electron and hole lifetimes in high purity Si, $\tau = 1x10^{-7}$ s, the carrier recombination is between 3-9% ($\eta_{rec}$ is between 91-97 %), depending on the amount of deposited energy and the incident height [16]. The electron and hole lifetimes are sensitive to the density of defect states, which can be due to poor material quality or impurities. Also, the incident alpha and $^{7}$Li ions will create crystal defects along their tracks, leading to decreased carrier lifetime after prolonged exposure to a high neutron flux. Larger pillar diameter generally leads to slightly less signal loss for a given lifetime (Figure 4). Since SRH recombination is proportional to the carrier density, the larger pillar volume of the 5 μm diameter pillar allows the charge cloud to diffuse farther laterally, resulting in an effectively lower carrier density.

Surface recombination can also play a role in reducing the detector efficiency. Unpassivated semiconductor surfaces have dangling bonds which can act as recombination centers. The density of these states can be increased by surface damage due to processing. Surface recombination velocity (S) is a function of the density of surface defects given by [17]:

$$S = \sigma \cdot \upsilon_{th} \cdot N_{st} \quad (3)$$

where $\sigma$ is the surface trap capture cross section, $\upsilon_{th}$ is the thermal velocity and $N_{st}$ is the number of surface trapping centers per unit area.

The effect of surface recombination velocity on carrier recombination for 25 μm tall pillars depends critically on pillar diameters and pitch (Figure 5). The amount of recombination increases for the smaller pillar diameters are due to a larger surface area to volume ratio. As the electrons and holes separate under the applied electric field, they also diffuse laterally and recombine at the edges more quickly for small diameter pillars. High surface recombination velocity can also cause increased reverse bias leakage current. This leads to a higher noise floor which requires an increase in the discriminator threshold and thereof reduces the overall efficiency. Surface recombination velocities of well-passivated surfaces are regularly reported to be ≤ 1000 cm/s [18-20]. At this level, surface recombination should not play a major role in efficiency reduction.

### B. Simulated efficiency

The simulated total efficiencies including all four efficiency components for several detector heights and geometries are shown in Figure 6. The efficiency scales with pillar height because a larger percentage of incident neutrons can interact with the $^{10}$B than in the case of planar detector design. The detection efficiency also scales inversely with diameter and pitch. For smaller pillar spacing, less energy is lost by the reaction by -products before hitting the Si pillars. For 1 μm diameter, 1 μm spacing and 100 μm height pillars, an efficiency of 75 % is predicted. It may be counter-intuitive that the efficiency continues to increase dramatically beyond heights greater than three times the mfp (54 μm). This is a consequence of the 4π neutron source in the simulation. Since many of the neutrons are not incident normal to the top surface of the detector, the probability that their paths only intersect the $^{10}$B portion of the detector is small. Thus, these neutrons may traverse through both $^{10}$B and Si and are expected to require a distance longer than three times the mfp in order to travel through sufficient thickness of $^{10}$B to interact.

### C. Gamma rejection

The simulated neutron to gamma rejection for gamma energies of 200 keV, 662 keV and 1 MeV are shown in Figure 8. The results show that the rejection ratio is in the range of $1x10^{5}$ - $4x10^{5}$ for all simulated geometries. The low gamma discrimination is due to the low linear attenuation coefficient (μ), which accounts for the probability of interaction per unit distance and (for the energies of interest, 100 keV to 2 MeV is Compton Scattering limited [10] and therefore the μ can be readily determined.) For the upper bound gamma energy of interest, γ = 2 MeV gives a μ = 0.10 $cm^{-1}$[10], which is dependent on the low atomic number Z = 14 and density ρ = 2.33 $g/cm^{3}$ of Si. The low μ, in addition to the thin device thickness or pillar height, is responsible for the very small gamma counts being registered and correspondingly large neutron to gamma discrimination.

## IV. Experimental Validation of Simulations

The efficiency was measured using a fission neutron source moderated by polyethylene blocks to yield thermal neutrons. The detection efficiency for 7 μm and 12 μm tall, 2 μm diameter pillars with 2 μm spacing detectors was measured to be 3.6 % and 7.3 % respectively at -2 V reverse bias. The measured devices required a discriminator value of 300 keV to reject the noise which is dominated by leakage current. Figure 9 shows the simulated effect of discriminator threshold on detection efficiency. When 300 keV is used for discriminator value, the simulated efficiency of 6.53 % is within 10 % of the measured efficiency at 7.3 % [5,8] for the 12 μm tall pillar array. Also a neutron to gamma discrimination of $10^{5}$ for 662 keV $^{137}$Cs gamma source [5] was measured for the 12 μm tall, 2 μm diameter pillars with 2 μm spacing which agrees well with the simulated value of 2 x $10^{5}$.

## V. Conclusion

The relationship between the geometrical features and thermal neutron detection efficiency in $^{10}$B based Si micropillar arrays was investigated by Monte Carlo radiation transport methods coupled with finite element drift-diffusion carrier transport simulations. The effects of pillar geometry, carrier lifetime and surface recombination velocity on the

collected signal were explored. It was found that for surface recombination velocities lower than $10^3$ cm/s and for electron and hole lifetime's longer than $10^{-7}$ s, less than 10% of the generated carriers recombine, thus having a small effect on the overall thermal neutron detection efficiency (1-4% depending on pillar geometry). The simulations predict an efficiency of 75 % for a 1 μm diameter, 1 μm spacing and 100 μm height pillar array using 100 keV discriminator threshold. Discrimination between neutron events and gamma events was also simulated for a 2 μm x 2 μm pillar array of various pillar heights. Good agreement was found between simulation and measurement when an appropriate discriminator value was used for the simulated efficiency calculation, providing a pathway to high efficiency solid state thermal neutron detectors of the future.

## ACKNOWLEDGMENT

The authors thank Catherine E. Reinhardt and Robert T. Graff for assistance processing of the neutron detectors.

## REFERENCES

[1] D. S. McGregor, S. L. Bellinger, D. Bruno, S. Cowley, M. Elazegui, W. J. McNeil, E. Patterson, T. Unruh, C. J. Solomon, J. K. Shultis, and B. B. Rice, "Perforated semiconductor neutron detector modules for detection of spontaneous fission neutrons," in *2007 IEEE Conference on Technologies for Homeland Security. Woburn, MA*, 2007, pp. 162-167.

[2] J. K. Shultis and D. S. McGregor, "Efficiencies of coated and perforated semiconductor neutron detectors," *IEEE Transactions on Nuclear Science,* vol. 53, pp. 1659-1665, 2006.

[3] K. Osberg, N. Schemm, S. Balkir, J. I. Brand, M. S. Hallbeck, P. A. Dowben, and M. W. Hoffman, "A handheld neutron-detection sensor system utilizing a new class of boron carbide diode," *IEEE Sensors J.,* vol. 6, pp. 1531-1538, 2006.

[4] J. Uher, C. Frojdh, J. Jakubek, C. Kenney, Z. Kohout, V. Linhart, S. Parker, S. Petersson, S. Pospisil, and G. Thungstrom, "Characterization of 3D thermal neutron semiconductor detectors," *Nuclear Instruments & Methods in Physics Research, Section A (Accelerators, Spectrometers, Detectors and Associated Equipment),* vol. 576, pp. 32-7, 2007.

[5] R. J. Nikolic, A. M. Conway, C. E. Reinhardt, R. T. Graff, T. F. Wang, N. Deo, and C. L. Cheung, "Pillar Structured Thermal Neutron Detector with 6:1 Aspect Ratio," *Applied Physics Letters,* submitted.

[6] A. S. Tremsin, W. B. Feller, and R. G. Downing, "Efficiency optimization of microchannel plate (MCP) neutron imaging detectors. I. Square channels with $^{10}$B doping," *Nuclear Instruments & Methods in Physics Research, Section A (Accelerators, Spectrometers, Detectors and Associated Equipment),* vol. 539, pp. 278-311, 2005.

[7] R. J. Nikolic, C. L. Cheung, C. E. Reinhardt, and T. F. Wang, "Roadmap for high efficiency solid-state neutron detectors." vol. 6013, no. 1 Boston, MA: SPIE - International Symposium on Integrated Optoelectronic Devices, Photonics West, 2005, pp. 36-44.

[8] R. J. Nikolic, A. M. Conway, C. E. Reinhardt, R. T. Graff, T. F. Wang, N. Deo, and C. L. Cheung, "Fabrication of Pillar-Structured Thermal Neutron Detectors," in *IEEE Nuclear Science Symposium, Conference record* Honolulu, Hawaii, Oct. 27-Nov. 3, 2007, pp. 1577-1580.

[9] N. Deo, J. R. Brewer, C. E. Reinhardt, R. J. Nikolic, and C. L. Cheung, "Conformal filling of silicon micro-pillar platform with 10boron," *J. Vac. Sci. Technol. B,* p. in press, 2008.

[10] N. Tsoulfanidis, *Measurement and Detection of Radiation, 2cnd ed*. Washington: Taylor & Francis, 1995.

[11] "MCNP4C - Monte Carlo N-Particle Transport Code System," Los Alamos National Laboratory, 2000.

[12] J. Ziegler, "SRIM – Stopping Range of Ions in Matter," 2006.

[13] R. D. Ryan, "Precision measurements of the ionization energy and its temperature variation in high purity silicon radiation detectors," in *19th Nuclear Science Symposium and the 4th Nuclear Power Symposium . Miami, FL*, 1973.

[14] D. S. Yaney, J. T. Nelson, and L. L. Vanskike, "Alpha-particle tracks in silicon and their effect on dynamic MOS RAM reliability," *IEEE Transactions on Electron Devices,* vol. ED-26, pp. 10-16, 1979.

[15] S. Kirkpatrick, "Modeling Diffusion and Collection of Charge from Ionizing Radiation in Silicon Devices," *IEEE Transactions on Electron Devices,* vol. 26, pp. 1742-1753, 1979.

[16] A. M. Conway, R. J. Nikolic, and T. F. Wang, "Numerical Simulations of Carrier Transport in Pillar Structured Solid State Thermal Neutron Detector," College Park, MD, December 12-14, 2007.

[17] G. F. Knoll, *Radiation Detection and Measurement 3rd. ed.* New York: John Wiley & Sons, Inc., 2000.

[18] G. Agostinelli, A. Delabie, P. Vitanov, Z. Alexieva, H. F. W. Dekkers, S. De Wolf, and G. Beaucarne, "Very low surface recombination velocities on p-type silicon wafers passivated with a dielectric with fixed negative charge," *Solar Energy Materials and Solar Cells,* vol. 90, pp. 3438-43, 2006.

[19] B. Hoex, F. J. J. Peeters, M. Creatore, M. A. Blauw, W. M. M. Kessels, and M. C. M. van de Sanden, "High-rate plasma-deposited $SiO_2$ films for surface passivation of crystalline silicon," *Journal of Vacuum Science & Technology A (Vacuum, Surfaces, and Films),* vol. 24, pp. 1823-30, 2006.

[20] O. Palais, M. Lemiti, J. F. Lelievre, and S. Martinuzzi, "Comparison of efficiencies of different surface passivations applied to crystalline silicon," *Diffusion and Defect Data Part B (Solid State Phenomena),* vol. 108-109, pp. 585-90, 2005.

[21] "Silvaco Atlas manual," Santa Clara: Silvaco International, 2007.

[22] A. H. Benny and F. D. Morten, "The Measurement of Surface Recombination Velocity on Silicon," *Proceedings of the Physical Society,* vol. 72, pp. 1007-1012, 1958.

**Figures**

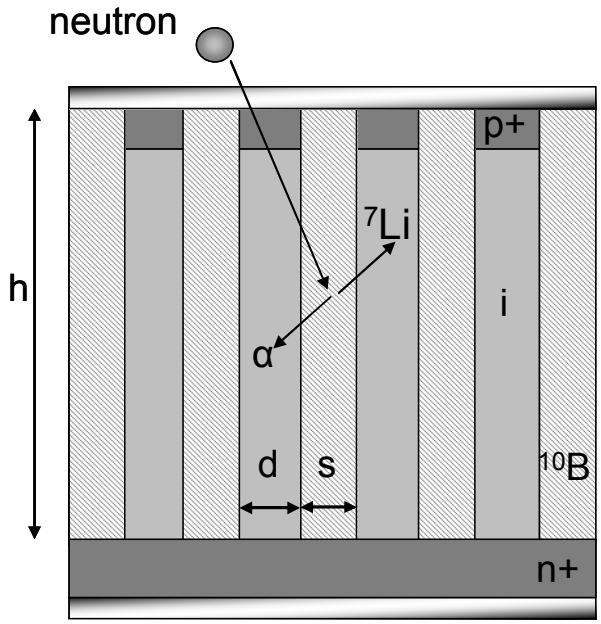


Figure 1. Schematic diagram of our 3-D pillar structured thermal neutron detector, with height (h), equal pillar diameter (d) and spacing (s), organized in a square lattice matrix.

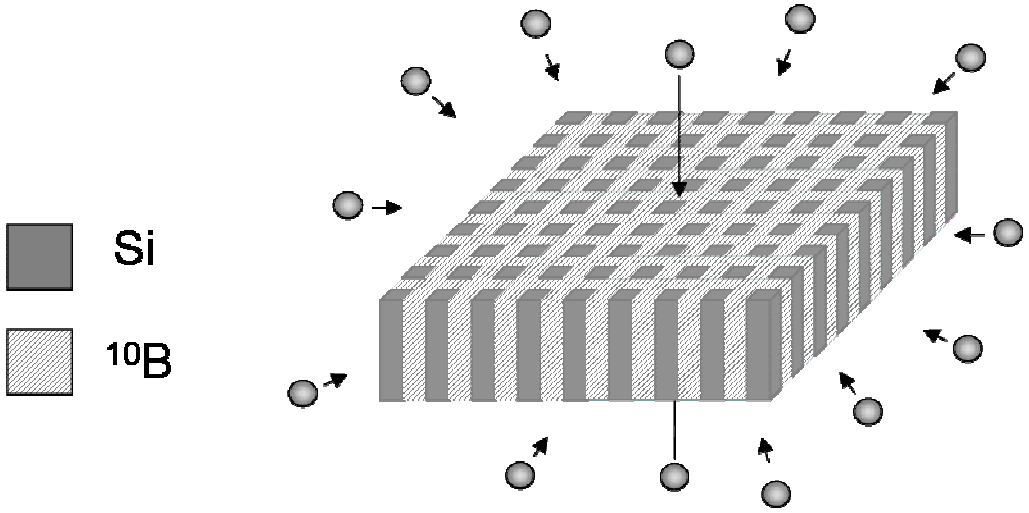


Figure 2. Neutrons incident on all sides (4π) of the array at all possible angles for MCNP simulations.

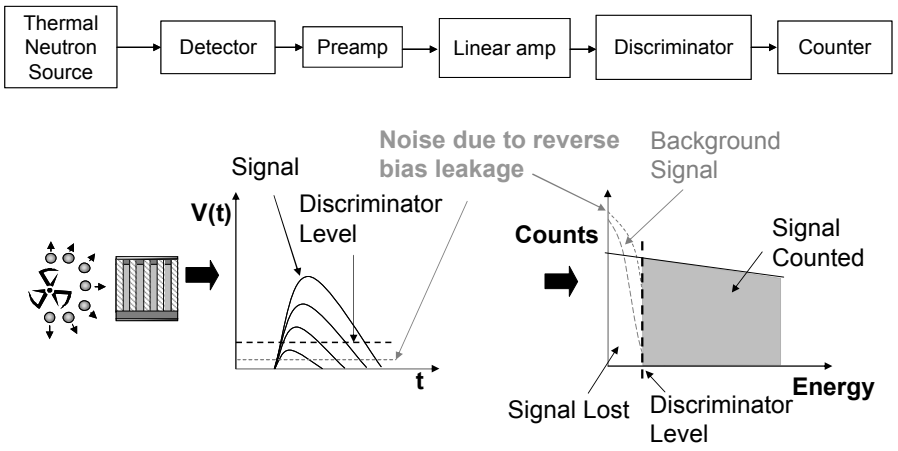


Figure 3. Schematic diagram of pillar structured thermal neutron detector.

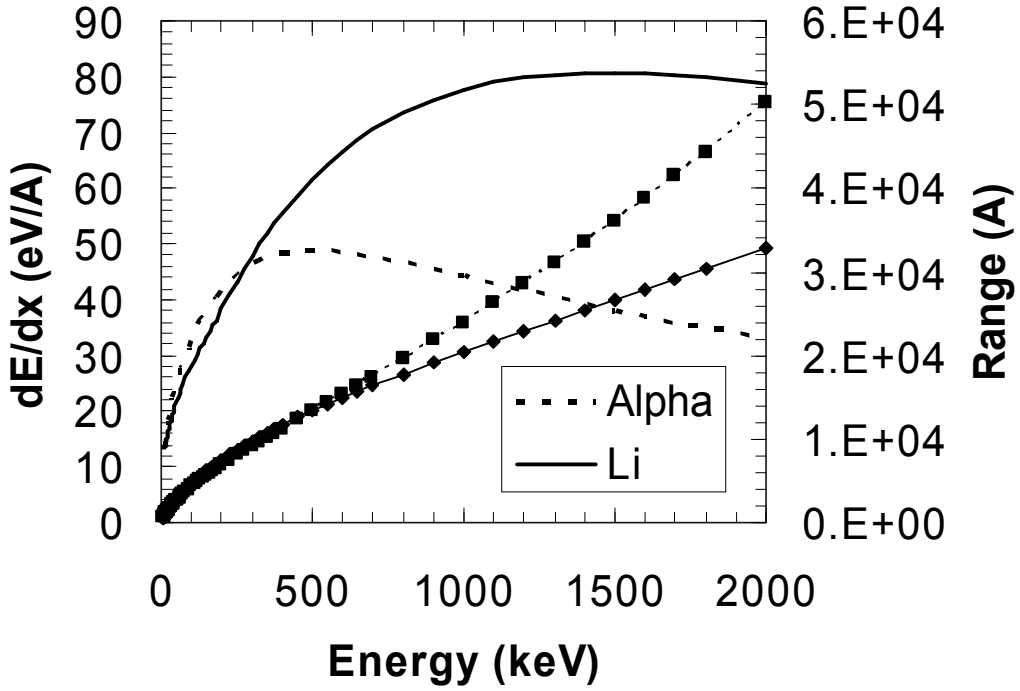


Figure 4. SRIM calculation of energy deposited in Si pillar as a function of energy for ionized alpha and $^{7}$Li particles and range in Si.

**Table I. Range of ions in $^{10}$B and Si**

| | 1st Excited State | | Ground State | |
|---|---|---|---|---|
| Ion | Alpha | Li | Alpha | Li |
| Energy (MeV) | 0.84 | 1.47 | 1.02 | 1.78 |
| Distance in $^{10}$B (μm) | 1.85 | 3.6 | 2.0 | 4.4 |
| Distance in Si (μm) | 2.4 | 5.2 | 2.8 | 6.4 |

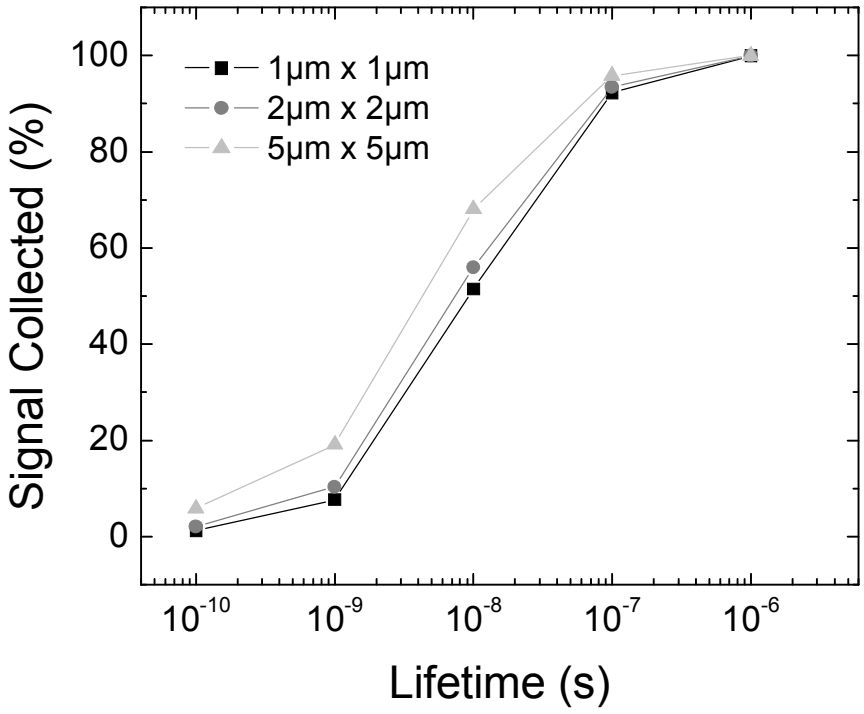


Figure 5. The effect of carrier lifetime on the percent of collected signal. Typical lifetimes for high quality Si are between $10^{-7}$ to $10^{-6}$ s [21].

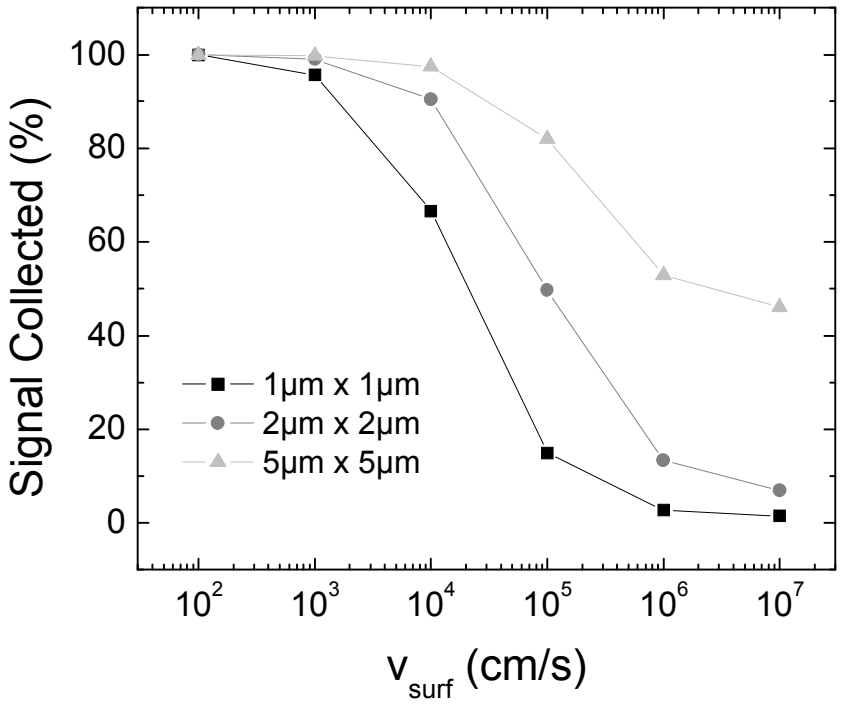


Figure 6. Effect of surface recombination velocity on the percent of collected signal. Typical values for Si surfaces range between 100 cm/s to $10^6$ cm/s [21, 22] depending on processing conditions and surface passivation techniques [18-20]. For small diameter pillars, the effect of surface recombination is a larger due to a larger surface area to volume ratio.

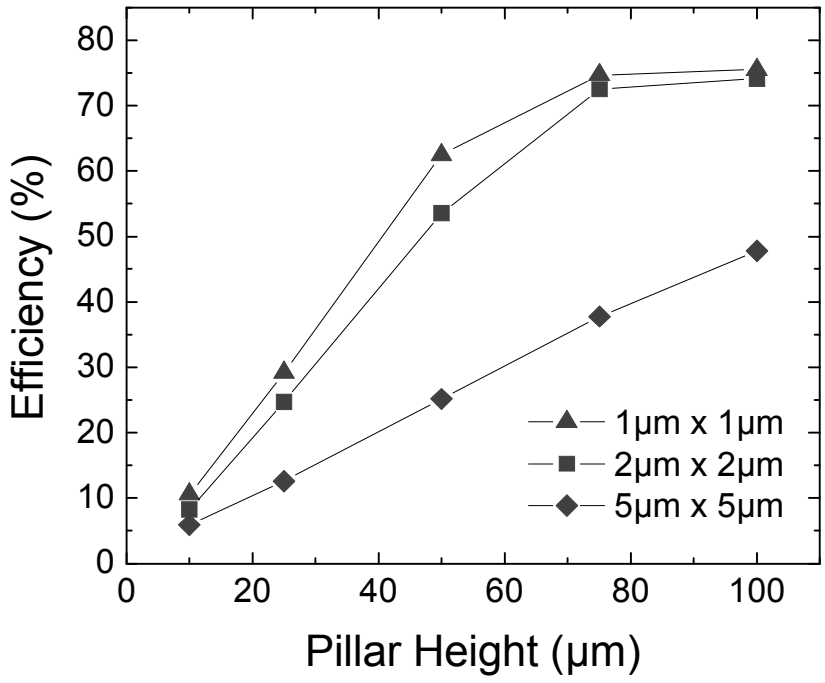


Figure 7. Simulated efficiency versus pillar height for various pillar geometries. This calculation includes all efficiency components ($\eta_{int}*\eta_{con}*\eta_{semi}*\eta_{rec}$) assuming 100 keV discriminator value, $1x10^{-7}$ s electron and hole lifetimes and a surface recombination velocity of $10^2$ cm/s.

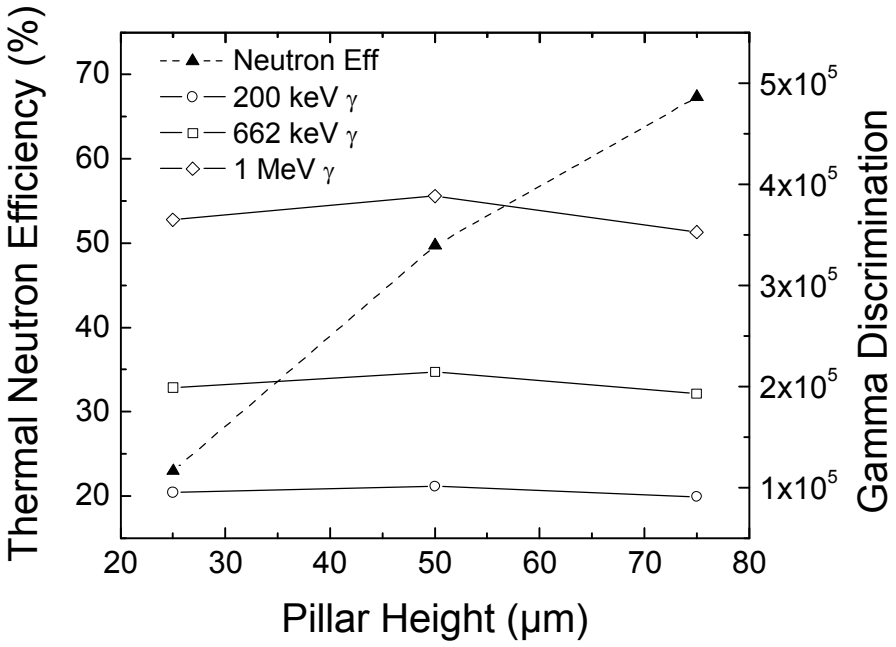


Figure 8. Simulated gamma to neutron discrimination for a pillar diameter of 2 μm and pillar separation of 2 μm versus pillar height. While the pillar height has little effect on the discrimination value, it has a large effect on the thermal neutron detection efficiency.

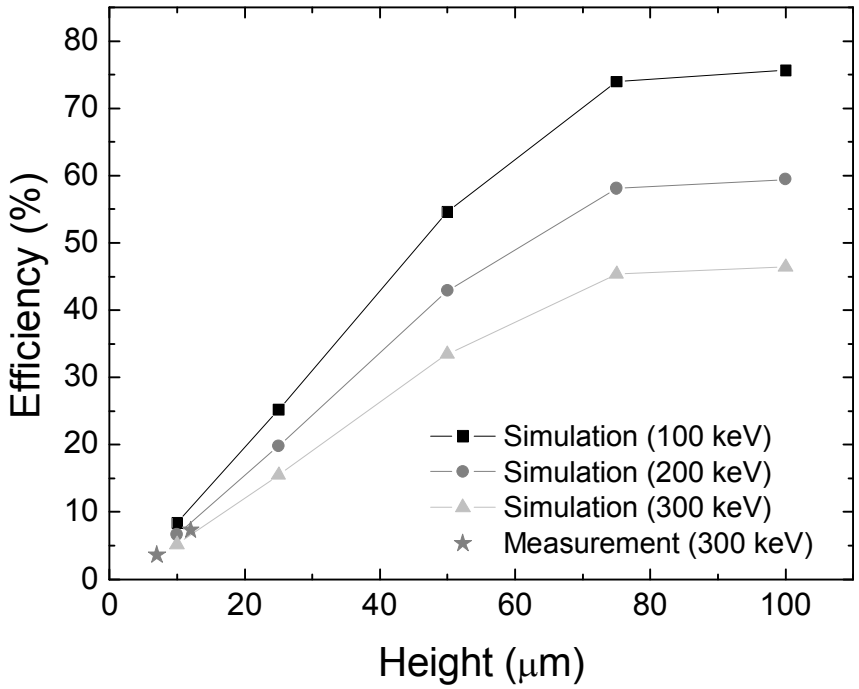


Figure 9. Comparison of simulated detection efficiency at various discriminator values overlaid with the measured detection efficiency for pillar array of 2 μm diameter and 2 μm spacing. At a discriminator threshold of 300 keV there is good agreement (10% error) between simulation and measurement.